



Fight the Flow: The Role of Shear in Artificial Rheotaxis for Individual and Collective Motion

Journal:	<i>Nanoscale</i>
Manuscript ID	NR-ART-12-2018-010257.R1
Article Type:	Paper
Date Submitted by the Author:	23-Apr-2019
Complete List of Authors:	<p>Baker, Remmi; Pennsylvania State University, material science and engineering Kauffman, Joshua; Pennsylvania State University, Department of Chemistry Laskar, Abhrajit; University of Pittsburgh, Chemical Engineering Shklyaev, Oleg; University of Pittsburgh, Chemical Engineering Potomkin, Mykhailo; Pennsylvania State University, Mathematics Dominguez-Rubio, Leonardo; Pennsylvania State University, Department of Biomedical Engineering Shum, Henry; University of Waterloo, Applied Mathematics Cruz-Rivera, Yareslie; Pennsylvania State University, Department of Chemistry Aranson, Igor; Pennsylvania State University, Department of Biomedical Engineering; Pennsylvania State University, Department of Chemistry; Pennsylvania State University, Department of Mathematics Balazs, Anna; University of Pittsburgh, Chemical Engineering Sen, Ayusman; Pennsylvania State University, Chemistry</p>

Cite this: DOI: 00.0000/xxxxxxxxxx

Fight the Flow: The Role of Shear in Artificial Rheotaxis for Individual and Collective Motion

Remmi Baker,^{a‡} Joshua E. Kauffman,^{*b‡} Abhrajit Laskar,^{c‡} Oleg E. ShklyaeV,^c Mykhailo Potomkin,^d Leonardo Dominguez-Rubio,^e Henry Shum,^f Yareslie Cruz-Rivera,^b Igor S. Aranson,^{*b,d,e} Anna C. Balazs,^{*c} Ayusman Sen^{*b}

Received Date
Accepted Date

DOI: 00.0000/xxxxxxxxxx

To navigate in complex fluid environments, swimming organisms like fish or bacteria often reorient their bodies antiparallel or against the flow, more commonly known as rheotaxis. This reorientation motion enables the organisms to migrate against the fluid flow, as observed in salmon swimming upstream to spawn. Rheotaxis can also be realized in artificial microswimmers—self-propelled particles that mimic swimming microorganisms. Here we study experimentally and by computer simulations the rheotaxis of self-propelled gold-platinum nanorods in microfluidic channels. We observed two distinct modes of artificial rheotaxis: a high shear domain near the bottom wall of the microfluidic channel and a low shear regime in the corners. Reduced fluid drag in the corners promotes the formation of many particle aggregates that rheotax collectively. Our study provides insight into the biomimetic functionality of artificial self-propelled nanorods for dynamic self-assembly and the delivery of payloads to targeted locations.

1 Introduction

In flowing fluids, many aquatic organisms actively reorient their bodies to swim against the flow direction.^{1–4} This motion is referred to as positive rheotaxis and allows the organisms to navigate moving currents.^{1–9} Positive rheotaxis also plays a vital role in the mammalian lifecycle. Specifically, the motile spermatozoa orient their axes antiparallel to the surrounding flow direction and move upstream. In the oviduct, this behavior helps guide sperms to the egg.⁸

There have been a few studies examining artificial rheotaxis in self-propelled particles.^{10–13} All previous studies observed the reorientation and behavior of individual microswimmers in a high shear domain next to a single wall.^{12,13} These *in situ* studies take place in environments that are very different from the proposed operating biological environments like blood vessels and capillaries.

Here, we employ both experimental and computer simulations to investigate individual and collective behaviors arising during rheotaxis. Specifically, the confinement within a microchannel enables us to observe changes in the individual and collective behaviors in rheotaxing particles across a wide range of shear rates. We determined that two distinct modes of rheotaxis exist at high and low shear rate regimes; these modes determine if an actively swimming particle can migrate upstream against the flow or follow as highly aligned particles along streamlines. Furthermore, we observed for the first time emergent collective behavior in artificially rheotaxing microswimmers. Our study highlights the specific role of shear and channel geometry for inducing artificial rheotaxis—pinpointing aspects that can be “tuned” for specific rheotactic functions and *in vivo* microfluidic applications.

2 Experimental Methodology

Microfluidic channels were fabricated from a Dow Sylgard 184 Polydimethylsiloxane (PDMS) Kit (1:5 curing ratio) using soft lithography. The negatively-charged microfluidic channels were

^a Department of Material Science and Engineering, The Pennsylvania State University, University Park, PA 16802, USA

^b Department of Chemistry, The Pennsylvania State University, University Park, PA 16802, USA

^c Department of Chemical Engineering, University of Pittsburgh, Pittsburgh, PA 15260, USA

^d Department of Applied Mathematics, The Pennsylvania State University, University Park, PA 16802, USA

^e Department of Biomedical Engineering, The Pennsylvania State University, University Park, PA 16802, USA

^f Department of Applied Mathematics, University of Waterloo, Waterloo, ON N2L 3G1, CA

Electronic Supplementary Information (ESI) available: [details of any supplementary information available should be included here]. See DOI: 00.0000/00000000.

‡These authors contributed equally to this work.

* Corresponding authors :

I. S. A. E-mail: isa12@psu.edu

A. C. B. E-mail: balazs@pitt.edu

A. S. E-mail: asen@psu.edu

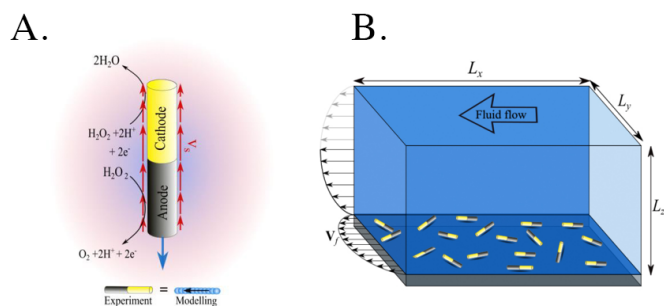


Fig. 1 Schematic of the Experimental and Computational Systems Cartoon of a chemically powered bimetallic nanorod. Different reactions occurring on two halves of the bimetallic rod form a gradient in proton concentration from head end to tail end. Each nanorod was modeled by a collection of elastically connected mesh-points (shown with blue spheres in the bottom inset) and hydrogen peroxide was consumed at constant rates at both ends. (B) A schematic of the microfluidic channel showing the settling plane of the nanorods, fluid flow directions and shear environments.

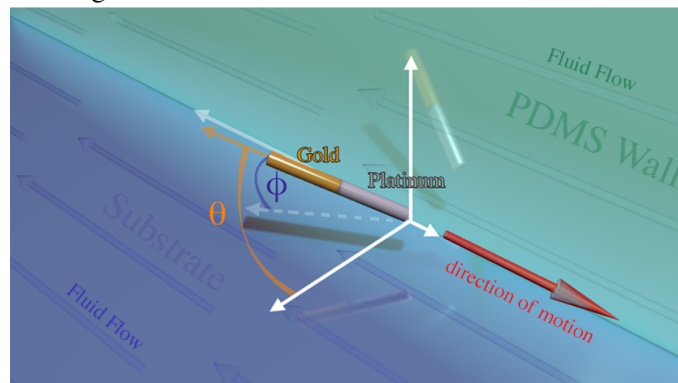
100 μm wide and 100 μm tall. We injected a colloidal suspension containing passive, negatively charged Au-Pt bimetallic (Figure 1A) nanorods into the channel. As time passes, the colloidal suspension separates and the nanorods naturally come to rest above the glass substrate (Figure 1B). To induce flow in the confined system, we connected the microfluidic channel with polyethylene tubing to a 250 μl Hamilton glass syringe on a Cetoni Low-Pressure precision nemeSYS syringe pump. The glass syringe was filled with either Millipore water or 30 v/v hydrogen peroxide. We varied the flow rate inside the microfluidic channel by adjusting the pumping rates from 1, 10, 100, to 1000 $\mu\text{l/hr}$ and observed the nanorods with an inverted Olympus microscope fitted with a 60x oil-immersion lens and redLED white light source. The videos were recorded using an Allied Vision ProSilica GT GIGE camera to capture up to 67 frames per second.

3 Experimental Results

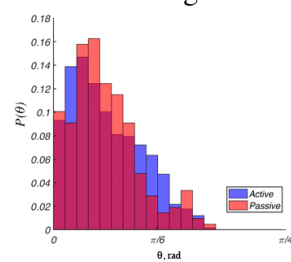
3.1 Inducing Artificial Rheotaxis

In the absence of hydrogen peroxide, the self-propelled Au-Pt nanorods act as passive particles—the particles follow streamlines in either parallel or antiparallel orientations. The introduction of hydrogen peroxide via externally imposed flow “activates” the self-propulsion mechanism (Figure 1A).^{14–17} The active bimetallic nanorods then produce a local dipole across the Au-Pt interface. While the entire nanorod maintains a negative zeta potential, there is a permanent separation of charges from the platinum head and gold tail.^{14–17} Near a surface with a negative zeta potential, e.g. glass substrate or PDMS side walls, the nanorods are repelled away from the surface to an equilibrium distance from the substrate (Figure 2A). Due to the charge separation across the Au-Pt interface, the nanorods also assume an equilibrium angle with respect to the substrate, i.e. the less negatively charged platinum head is closer to the substrate than the more negatively-charged gold tail. We define two equilibrium angles for the nanorods as a vertical angle (θ) and horizontal angle (ϕ) (Figure 2A). We find through image processing for the vertical

A. Diagram of a Nanorod in Solution



B. Vertical Angle



C. Horizontal Angle

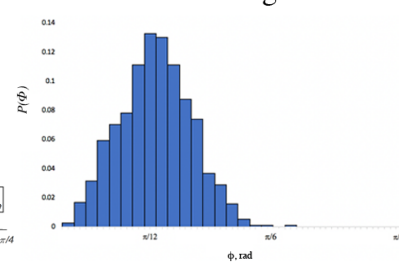


Fig. 2 Rheotaxis Reorientation Angles (A) A schematic illustrating the forces and torques along a tilted Au-Pt bimetallic nanorod in a moving fluid. (B) The distribution of vertical angles θ of both passive and active nanorods. (C) The distribution of horizontal angles ϕ for active and positively rheotaxing nanorods along the microfluidic corners. We find a $\theta_{ave} \sim 21.5^\circ$ (0.367 rad) and $\phi_{ave} \sim 16^\circ$ (0.279 rad) for the vertical and horizontal angles respectively.

angle $\theta \sim 21.5^\circ$ and the horizontal angle $\phi \sim 16^\circ$. The equilibrium vertical and horizontal angles are not equal due to the difference in the negative zeta potentials at the glass substrate and PDMS side walls (Figure 2B-C).

As a point of reference, we compare the measured values of the vertical angles for active and passive (i.e. no hydrogen peroxide) nanorods. The average angle for active and passive nanorods is $\theta_{active} \sim 21.5^\circ$ and $\theta_{passive} \sim 21.8^\circ$, respectively (Figure 2B). While the angles for active and passive rods lie within experimental error, the angle distribution for passive rods is noticeably wider. We presume the similarity in vertical angles is due to a light-induced thermophoretic effect across both passive and active nanorods. Previous studies have shown gold nanoparticles have enhanced diffusion in the presence of particular wavelengths. Since we are using a strong white LED light source, we hypothesize the gold tail is heating and creating a temperature gradient along the length of the nanorod. The combination of electrical repulsion from substrate to nanorod and the temperature gradient from the platinum to gold segments, the nanorod creates an angle relative to the substrate (and by extension light source).

Furthermore, a light-induced thermophoretic effect also accounts for the observed anomalies between passive and active nanorods. We firstly observe that active particles have a slightly smaller vertical angle. Active particles may transfer localized heat

more effectively from the gold segment into the environment because of the induced electro-osmosis flows. As a result, the active particles experience less of a temperature gradient along the length of their bodies. In the presence of the dominating self-electrophoretic effects, thermophoresis may be ignored for active particles.

However, for passive particles we cannot ignore thermophoretic effects. We observe higher diffusion for rotation ($D_r \sim 1.1\text{--}1.2 \text{ sec}^{-1}$) when compared to theoretical predictions. The presence of defects in the passive nanorods, e.g. nanorod length or segment thicknesses, can drastically affect individual thermophoretic effects. Hence, we observe a wider distribution of vertical angles when compared to active particles.

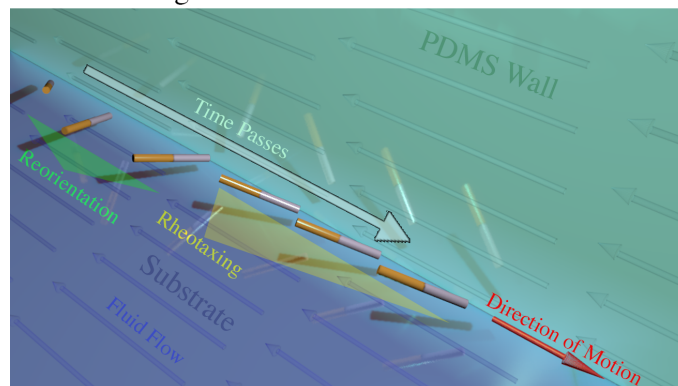
The localization of the nanorods near the bottom surface (when compared to a disperse colloidal nanorod solution) leads to a very different response to shear. The imposed fluid flow has a shear gradient along the length of the tilted nanorod. The nanorod responds to the dynamic environment by reorienting its body antiparallel to the fluid flow (Figure 3A). The active particle remains at the equilibrium distance away from the surface and maintains the vertical angle (θ) with the glass substrate due to localized electro-osmosis flows around the particle and the force-balance between repulsion from the substrate and gravity.

The shear stress in the fluid changes abruptly from high shear in the center of the bottom wall to low shear at the corners. Our experimental setup can be assumed to be a steady-state, incompressible fluid flowing under a constant pressure gradient—a problem solved in depth.^{18–21} The solutions for shear stress in the corners in a microfluidic channel, are always zero. Hence, we arrive at the cross-sectional diagram for shear stress across the entire microfluidic channel (Figure 3B).

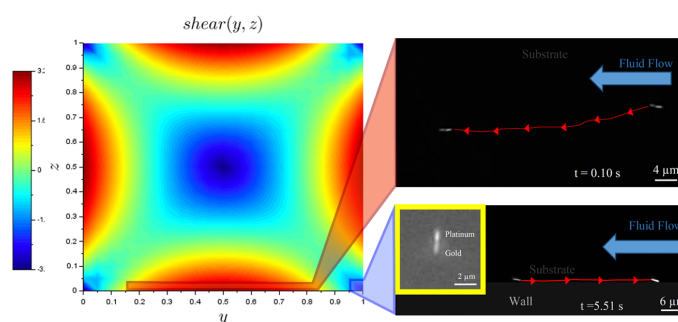
Thus, fluid shearing gives rise to two modes of artificial rheotaxis: low at the corners and high at the walls. As a result of changing shear across their body, the swimming particles preferentially reorient antiparallel to the flow, regardless of the shear strength. (Figure 3B). We observe two distinct behaviors of antiparallel nanorods as dependent upon the shear strength. In high shear the active nanorods follow the fluid streamlines, otherwise known as negative rheotaxis; or in a low shear environment where the fluid flow rate is small, active nanorods can migrate upstream in an antiparallel orientation, also called positive rheotaxis. Nanorods in the center of the channel are only stabilized in one direction (z -direction) with the vertical angle θ —an observation akin to rotational quenching^{22,23}—as such, the particles are sensitive to external fluctuations. Hence, we observe rheotaxing nanorods frequently “flipping out of plane”; in doing so, the particles destabilize and lose their preferred antiparallel orientation. The particles can regain their stable antiparallel orientation as they re-approach the substrate to rheotax.

A second artificial rheotaxis mode occurs in a low shear environment along the corners. Active particles approaching the corners reorient antiparallel at stable vertical and horizontal angles (Figure 2B-C). The vertical and horizontal angles oscillate around their respective average due to noise and fluctuations in the system. Additionally, the particles are hydrodynamically entrapped^{11,24} near the low-shear corner and will remain there

A. Reorienting for Rheotaxis



B. Shear Influences on Rheotaxis



C. Rheotaxis Velocity over Time

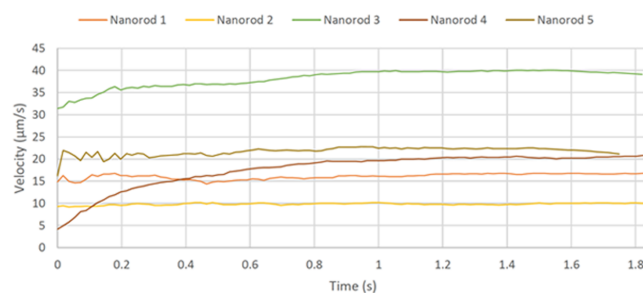


Fig. 3 Rheotaxis Modes (A) An illustration of the reorientation of a bimetallic nanorod. After reorienting, the nanorod positively rheotaxes upstream. (B) The magnitude of shear from the y - z cross section of the microfluidic channel is simulated. Two distinct regions of shear are shown: low shear in the corners and high shear along the center of the microfluidic channel. Regardless of the shear magnitude, the active nanorods will reorient antiparallel to the flow. In high shear, nanorods negatively rheotax with the fluid flow; by contrast, in low shear the active particles and effectively swim upstream against the flow. (C) The individual rheotaxing velocities for the same nanorods in Figure 3C are analyzed over time. The velocities increase over time as the swimming particles orient towards stable vertical and horizontal angles.

unless they collide with an obstacle (e.g. a wall defect) or another particle. As a result of the stabilized 3-D orientation and entrapment, the antiparallel particles swim at near constant velocities against large flow rates, i.e. positively rheotax (Figure 3C) (SIVideo1).

3.2 Emergent Collective Behavior

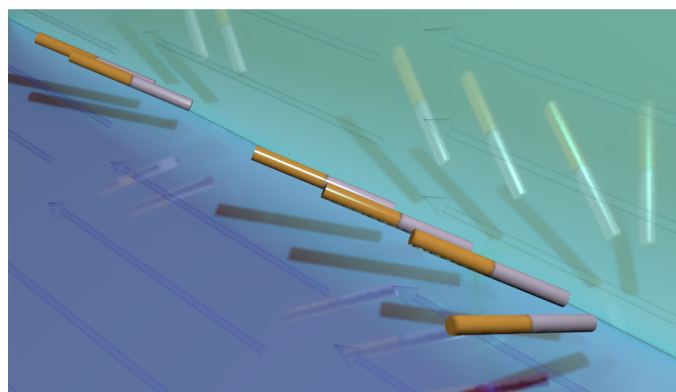
Additionally, we observe for the first time collective rheotaxis in artificial systems. The cooperative behavior occurs in the low shear at the channel corners, where individual nanorods can positively rheotax for long time scales without disruption. Differences in the structures of individual nanorods lead to a distribution of velocities and, combined with the hydrodynamic entrapment in low-shear environments, the nanorods concentrate along the corners. The active rheotaxing particles self-assemble in long chains (Figure 4A) (SIVideo2). Within the chains, the individual particles attain an equilibrium distance that permits the particles to actively consume fuel, while being repelled from both the nearby surfaces and neighboring particles. These swimming particles continually “tune” their neighboring distances and angles in order to preserve the center of mass velocity for the linear chain (Figure 4B). Time evolution of cluster formation is illustrated in Figures 4C,D. As one sees from the figures, the median cluster velocity decreases with the increase of number of particles in the cluster. This effect is probably due to enhanced fuel consumption by the cluster compared to individual rods.

Channel heterogeneity and noise (from temperature fluctuations and microbubble formation/bursting within the microfluidic channel) can disrupt the collective behavior and transform a linear rheotaxing aggregate into a disordered cluster. Disordered clusters consisting of a few particles (i.e. bimetallic nanorod dimers or trimers) rheotax slowly, remain stationary, or follow streamlines depending upon the arrangement of active particles (Figure 5). Polar particle aggregates exhibit positive rheotaxis. By contrast, a symmetric but disordered cluster shows negative rheotaxis in low-shear environments; in part because of the cancelling self-propulsion of opposing nanorods (SIVideo3). The larger agglomerates remain stationary at the corners and form localized regions where the chemicals are depleted from the solution. The chemical depletion prevents individual rheotaxing particles from circumventing the obstacle and results in the individual swimmers being “absorbed” into the disordered cluster. These findings on the effects of fluctuations and noise imply that external fields, e.g. acoustic or electric fields, could be used to control individual and collective behaviors.

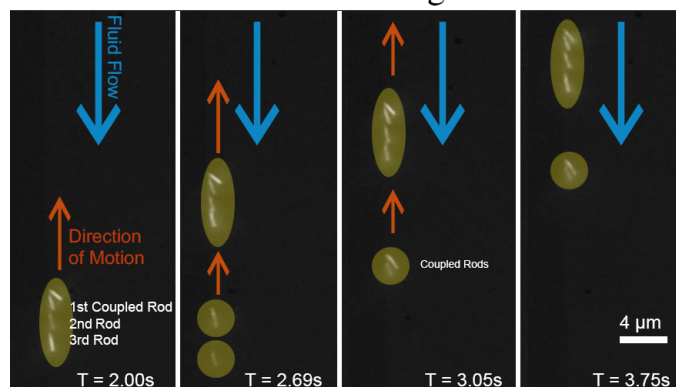
4 Computational Model

We developed a computational model to predict the rheotactic behavior of individual rods and multi-rod clusters. We simulate an individual nanorod as a collection of elastically-connected mesh points, i.e. spheres (Figure 1A) near an impermeable boundary^{22,23,25–27}. The simulated nanorods have a total length l , diameter d , and self-propelled velocity V_{sp} . We include a repulsive potential $U(r)$ to maintain the nanorods at an equilibrium height $h \sim 1 \mu\text{m}$ above the substrate.^{13,28} The inclusion of the repulsive

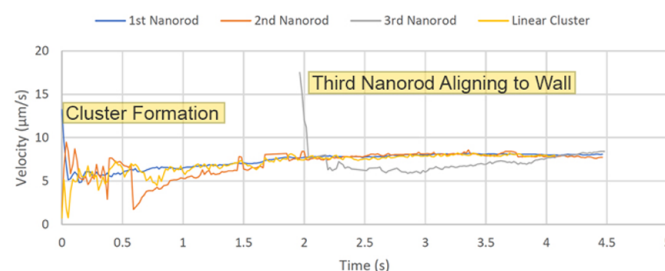
A. Collective Rheotaxis Diagram



B. Collective Rheotaxis Diagram



C. Cluster Positive Rheotaxis Velocities



D. Cluster Size vs Median Velocity

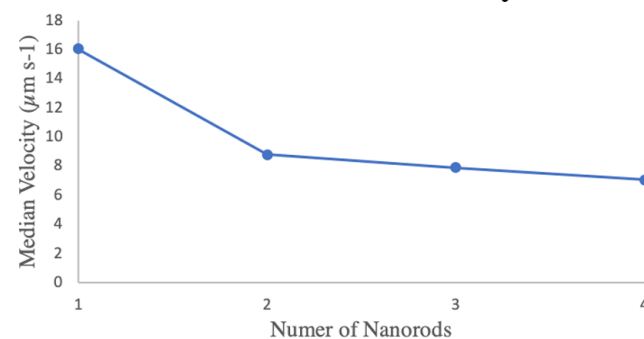


Fig. 4 Collective Motion (A) A cartoon illustrating the orientation of the individual nanorods in a collective and ordered “train.” (B) A time-lapse of a linearly ordered nanorod cluster along a low-shear corner of the microfluidic channel. The first two rods of the cluster are coupled together and analyzed as a single nanorod for simplicity. (C) The evolution of velocities is plotted for the aforementioned three-particle linear cluster as individual particles and a collective entity. (D) Dimers, trimers, and tetramers and their median velocities.

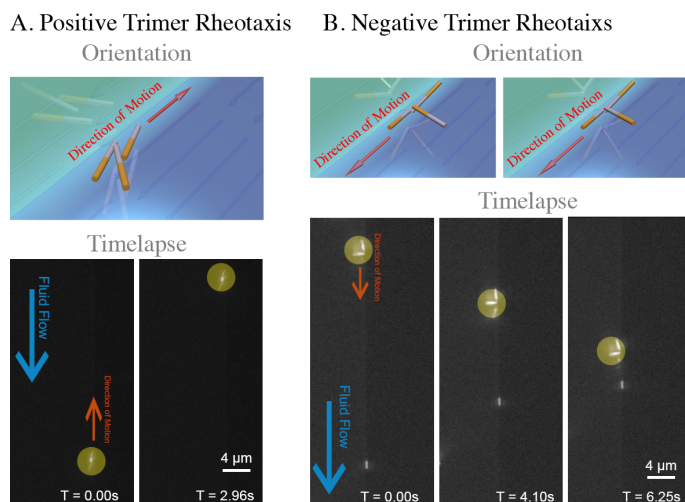


Fig. 5 Experimental Observations of Rheotaxing Clusters The timelapse images of two different disordered clusters are shown. Each cluster consists of an active trimer in a low-shear environment along the microfluidic corners. (A) For polar ordered, non-symmetric clusters, we observe positive rheotaxis. (B) By contrast for a symmetric but disordered cluster, we observe negative rheotaxis in low-shear environments.

potential closely mirrors the self-induced dipole arising in swimming, self-electrophoretic nanorods.

We also model the chemical kinetics and motility of a single nanorod according to Moran and Posner.^{14,25–27} The above method provides a set of nonlinear partial differential equations that take into account the fluid motion, the reaction-induced creation and transformation of different charged species, the arising dynamic electric field, and the migration of the species in the resultant electric field. This method also captures chemical species dynamics using a set of Nerst-Planck equations.¹⁴ We utilize their scaling arguments¹⁴ to establish a relationship between the velocity of the self-propelled rod and the concentration of fuel in the surrounding fluid. (See Supplemental Information for a full realization of the chemical kinetics responsible for the self-propulsion).

To capture the experimentally observed vertical and horizontal angles, θ and ϕ respectively, we impose an external torque across the length of the nanorod: $\Omega^w(\theta) = -C_w\Gamma(\Phi - \Phi_{eq})$ Here Φ refers to either vertical angle θ or horizontal angle ϕ because of the equilibrium condition $\Phi = \theta = \phi$, with the value of $\Phi \sim 10 - 20^\circ$. The magnitude of the coefficient accounts for the strength of the torque as a function of the distance of the rod from the wall. Following Das et al.,²² we assume a functional form $\Gamma(h) \propto (\frac{b}{b+h})^3$, where length b is half of the rod's total length l and height h is the distance of the center of mass of the rod from the wall. We set the cut-off distance as $R = 2 \mu\text{m}$ from the walls. The proportionality constant C_w accounts for the geometry of the swimmer and the interaction details.

To replicate the experimental design, we initially assign randomized positions and orientations to the nanorods, while avoiding any overlap among neighboring particles. We also simulated up to twenty ($N = 10, 20$) nanorods to analyze the emergent collective behavior. We then model the moving background

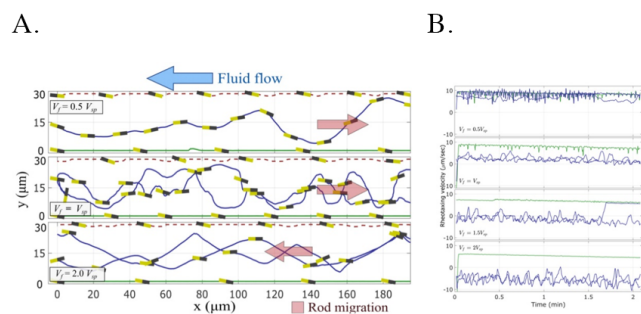


Fig. 6 Computational Modeling of Artificial Rheotaxis (A) Sample trajectories from the ten-rod simulations at different background flow strengths V_f . The direction of the nanorods' net migration through the middle of the channel is shown with red arrows. We observe a change from positive to negative rheotaxis as a result of a higher imposed fluid flow V_f . The trajectories of the non-rheotaxing particles are indicated by the dashed red line. (B) The evolution of the x-component of the velocities of rheotaxing rods is shown for different background fluid velocities. Green and blue lines indicate the respective velocities of rods rheotaxing along the corners and bulk of the channel.

fluid, otherwise referred as the characteristic fluid, in the Stokes limit (Reynolds number $Re \sim 2 \times 10^{-5}$) with the characteristics of a Poiseuille flow. We vary the characteristic fluid velocity V_f as a multiple of the nanorod's self-propulsion velocity V_{sp} .

5 Computational Results

We computed the effect of the vertical and horizontal angles, θ and ϕ respectively, for both positive and negative rheotaxis. Similar to the experiments, we consider two rheotaxis modes, whereby the nanorods are either in a high or low shear environment. In the first mode where shear is high, the vertical angle stabilizes the spacial orientation of the nanorods to prevent oscillations. To understand the stabilization effect arising from the vertical angle, we consider two cases: $\Phi_1 = 0$ and $\Phi_2 = \theta_{eq}$. In the absence of a vertical angle ($\Phi_1 = 0$), the nanorod hovers above substrate at an equilibrium height, and the imposed horizontal shear flow profile $v_x(y)$ causes the nanorod to rotate around its long axis. The flow forces the active nanorod to reorient towards the central line of the microfluidic channel; eventually giving rise to an oscillatory motion across this line. The swinging motion is caused by a non-uniform shear imposed by the Poiseuille flow and first analyzed by Zöttle et al.²⁹ Namely, the shear varies from low to high from the bulk of the channel to the side walls. This shear profile reorients the head of the rod toward the center line of the channel and, thus, causes the swinging motion. During this motion, the rod's trajectory repeatedly passes from one half of the channel to the other half. If the amplitude of this swinging motion is sufficiently large, the rod can reach the opposite walls. Along such trajectories, the rods spend some portions of time rheotaxing along the side walls and through the bulk between the walls. The rheotaxis along the side wall, however, is unstable due to the high shear imposed by the Poiseuille flow. See the supplemental information for more details.

By contrast when $\Phi_2 = \theta_{eq}$, the vertically-tilted nanorod experiences a differential fluid drag across the length of its body from

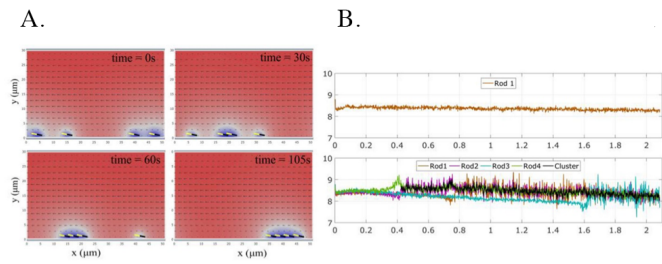


Fig. 7 Rheotaxing Clusters Without an Electrostatic Term (A) A sequence of snapshots illustrating the formation of a linear cluster by nanorods rheotaxing along the channel corner. The fluid flow V_f from right to left, as indicated by the grey arrows. (B) The evolution of the velocity of a single rod (top panel) and velocities of individual rods (bottom panel) sequentially merging into a linear cluster shown in (A). The slow decrease in the speed of the single rheotaxing rod is due to the depletion of the hydrogen peroxide in the solution. The velocities of individual rods, presented with lines of different colors, display small jumps as the rods merge into the cluster shown with a black line. The cluster velocity is defined as the average velocity of the constituent rods.

the imposed vertical flow $v_x(z)$. The elevated part of the rod (tail) in the planar Poiseuille flow experiences higher drag than the lower part (head) –producing an additional shear-induced hydrodynamic torque T_l^h that reorients the nanorod antiparallel to the flow. This flow-induced reorientation along centerlines is analogous to motile spermatozoa in complex flowing fluids. Furthermore, we can harness the reorientation near surfaces to analyze the shear rates and directionality of fluid flows, i.e. use swimming nanorods as *in-situ* "weather vanes."¹¹

Intrigued by the concept of using nanorods as *in situ* weather vanes, we analyzed the the orbital motion of the nanorods. We followed the predictions made by Uspal et al.¹¹ for the stabilizing the orbital rotation in Janus spheres, and expanded their model to account for elongated Janus particles, such as bimetallic nanorods in this study. We observe the combination of two torques arising from the vertical angle significantly dampens the oscillatory motion across the centerline. Over time, fluctuations resulting in the nanorods' rotational diffusion, inhomogeneities in the hydrogen peroxide concentration, and collisions among nanorods result in the upstream cross-stream migration of nanorods from high to low shear regimes (Figure 6A) (SIVideo4). The computationally and experimentally observed upstream cross-migration of our artificial swimmers is qualitatively and quantitatively similar to that in previously published studies on down-stream cross-migration of Janus spheres by Katuri et al.³⁰ and expulsion of bacteria in vortical flows from Sokolov et al.³¹

We also analyze how the behavior of the nanorods changes as they migrate from a high to low shear regions, i.e. from the center to corners of the microfluidic channel. In this second mode where the shearing rate is small along the corners, the nanorod establishes two non-zero equilibrium angles relative to the substrate and wall. Let us focus on the influence of the horizontal angle ϕ . The horizontal angle ϕ is the result of electrostatic and hydrodynamic interactions near the PDMS wall. The addition of the horizontal angle further stabilizes the orbital motion of the nanorods; giving rise to sustain trajectories with near constant

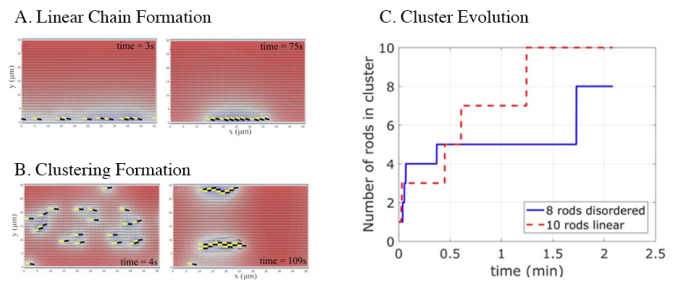


Fig. 8 Rheotaxing Clusters With an Electrostatic Term (A) Time-lapse of electrostatically interacting nanorods self-assembling into a linear aggregate. (B) A timelapse of the formation of clusters with electrostatically interacting nanorods. (C) A graphical comparison for the rates of formation for a linear chain and an asymmetric aggregate.

velocities (Figure 6A-B).

The behavior of particles in the two rheotaxis modes becomes apparent with variations in characteristic background flow V_f (SIVideo5). For sufficiently small background flows where self-propulsion velocity V_{sp} is greater than the characteristic flow V_f , we only observe one behavioral mode, positive rheotaxis. Nearly all the nanorods migrate upstream because the entire microfluidic channel is low shear (Figure 6B). However in strong characteristic flows, we observe the two behavioral modes, positive and negative rheotaxis, as dependent upon the shearing regime. In the first mode where shear is high along the center of the channel, the nanorods will drift with the fluid downstream because the characteristic fluid flow V_f is greater than the self-propulsion velocity V_{sp} . Conversely for low shear domains, the observe upstream migration in the corners because the self-propulsion velocity V_{sp} is greater than the characteristic flow V_f . Thus with slight adjustments to the strength of the background flow we can tailor the individual behavior of the nanorods for specific tasks, such as cargo pick-up and delivery.

Our model also captures the emergent collective behaviors of many artificially rheotaxing nanorods. First, nanorods migrate cross-stream from high to low shear regimes and adjust their spatial swimming orientation accordingly. The distance between two actively swimming nanorods decreases due to external fluctuations and noise, chemical concentration inhomogeneities, and particle-particle hydrodynamic interactions. These contributing factors lead to the formation of dimers and trimers (Figure 7A). We observe the small jumps in the velocities of individual as they merge into a collective, linearly ordered structure (Figure 7A). The inclusion of an electrostatic interaction term drastically destabilizes the linearly ordered chain, but does not affect the rate at which the train grows (Figure 8A).

Thus, with the inclusion of an electrostatic term, small fluctuations in the system, such as disturbances in the fluid flow and chemical gradients, transform the rheotaxing nanorod train into complex aggregates. These complex aggregates identify as being asymmetric or symmetric around the long axis of the cluster (Figure 8B). As observed in experiments, the simulated microstructures show rheotactic behavior for both symmetric and asymmetric clusters (Figure 8C). However, when we compare the

evolution for linear chains and aggregates, we observe a slower rate of formation for the aggregates (Figure 8D). The slower rate of formation is attributed to a local chemical depletion zone that starves internal nanorods of fuel and decreases their motility, similar to that observed in experiment (Figure. 4D). Thus, the aggregates can only grow when more motile nanorods or smaller cluster approaches. These observations for cluster growth are qualitatively similar to experiments. Thus, validated computational model can be used for the prediction and design of desired functions of active rods in microfluidic environment.

6 Summary

We experimentally and computationally studied artificial rheotaxis in a confined system. We find the coupling of hydroelectrodynamic fluid flows and electrostatic interactions with nearby surfaces induces a vertical and horizontal tilt in the self-propelled nanorod. The induced tilt and moving background fluid creates a differential fluid drag across the length of the nanorod—drastically affecting individual and collective behaviors. We study two distinct cases to better understand how the artificial rheotactic behavior continuously changes from a high shear environment in the center of the channel to a low shear domain near the corners. We critically find that negative rheotaxis occurs in the fluid bulk (or center of the channel). As nanorods migrate towards the corners, we observe a change from negative to positive rheotaxis.

The experimental and computational observations suggest that our observations for artificial rheotaxis in nanorods might be extended to other self-propelled Janus micromotors like as Janus spheres or microrockets.³² For the first time we observe emergent collective behavior in artificially rheotaxing microswimmers. In the corner regions where shear rates are small, the active particles self-assemble into linear aggregates, i.e. trains of nanorods swimming antiparallel to the fluid flow. The trains of nanorods are dynamically unstable due to electrostatic interactions of closely clustered actively swimming particles. Inhomogeneities and external noise lead to the breakdown of linear trains into disordered clusters. Depending on the symmetry of the disordered cluster, i.e. symmetric or asymmetric, we could observe both positive and negative rheotaxis.

Furthermore, we can exploit the emergent collective behaviors of artificially rheotaxing particles for on-demand and self-assembling mesoscale structures.^{33,34} The formation and behaviors of these dynamic and actively swimming mesoscale structures can be programmed during nanoparticle fabrication. For example, bimetallic nanorods can be fabricated with specific head-tail proportions, selective metallic materials, and active tuning *in situ* through fuel concentration and applied external fields. The tuning of interactions in a collective, artificial rheotaxing system provides an enhanced pathway for advancing targeted cargo delivery in the presence of fluid flow.

Conflicts of interest

The authors declare there are no conflicts of interest.

Acknowledgements

This research was supported by Penn State MRSEC under NSF grant DMR-1420620 (A. S) and grant DMR-1735700 (I. S. A.). We also acknowledge support from the NSF DMREF grant 1626742 (A. C. B.) at the University of Pittsburgh. We also would like to acknowledge the Center for Nanoscale Science, Materials Research Institute, and their staff at the Pennsylvania State University for their contributions. Lastly, we thank F. D. C. Isaac (Penn State) and F. C. Pepito (L'École de Physique des Houches) for their contributions in editing and discussions.

Notes and references

- 1 J. C. Montgomery, C. F. Baker and A. G. Carton, *Nature*, 1997, **389**, 960.
- 2 T. Kaya and H. Koser, *Biophysical journal*, 2012, **102**, 1514–1523.
- 3 H. Marcos and T. Fu, *Proc. Natl. Acad. Sci. USA*, 2012, **109**, 11.
- 4 N. Figueroa-Morales, G. L. Mino, A. Rivera, R. Caballero, E. Clément, E. Altshuler and A. Lindner, *Soft Matter*, 2015, **11**, 6284–6293.
- 5 M. Ramia, D. Tullock and N. Phan-Thien, *Biophysical journal*, 1993, **65**, 755–778.
- 6 P. D. Frymier, R. M. Ford, H. C. Berg and P. T. Cummings, *Proceedings of the National Academy of Sciences*, 1995, **92**, 6195–6199.
- 7 M. A.-S. Vigeant, R. M. Ford, M. Wagner and L. K. Tamm, *Appl. Environ. Microbiol.*, 2002, **68**, 2794–2801.
- 8 V. Kantsler, J. Dunkel, M. Blayney and R. E. Goldstein, *Elife*, 2014, **3**, e02403.
- 9 J. Hill, O. Kalkanci, J. L. McMurry and H. Koser, *Physical review letters*, 2007, **98**, 068101.
- 10 M. Potomkin, A. Kaiser, L. Berlyand and I. S. Aranson, *New Journal of Physics*, 2017, **19**, 115005.
- 11 W. Uspal, M. N. Popescu, S. Dietrich and M. Tasinkevych, *Soft Matter*, 2015, **11**, 6613–6632.
- 12 J. Palacci, S. Sacanna, A. Abramian, J. Barral, K. Hanson, A. Y. Grosberg, D. J. Pine and P. M. Chaikin, *Science advances*, 2015, **1**, e1400214.
- 13 L. Ren, D. Zhou, Z. Mao, P. Xu, T. J. Huang and T. E. Mallouk, *ACS Nano*, 2017, **11**, 10591–10598.
- 14 J. L. Moran and J. D. Posner, *Journal of Fluid Mechanics*, 2011, **680**, 31–66.
- 15 Y. Wang, R. M. Hernandez, D. J. Bartlett, J. M. Bingham, T. R. Kline, A. Sen and T. E. Mallouk, *Langmuir*, 2006, **22**, 10451–10456.
- 16 W. Wang, T.-Y. Chiang, D. Velegol and T. E. Mallouk, *Journal of the American Chemical Society*, 2013, **135**, 10557–10565.
- 17 W. F. Paxton, K. C. Kistler, C. C. Olmeda, A. Sen, S. K. St. Angelo, Y. Cao, T. E. Mallouk, P. E. Lammert and V. H. Crespi, *Journal of the American Chemical Society*, 2004, **126**, 13424–13431.
- 18 X. Qi, D. Scott and D. Wilson, *Chemical Engineering Science*, 2008, **63**, 2682–2689.

- 19 C. Fan and B.-T. Chao, *Zeitschrift für angewandte Mathematik und Physik ZAMP*, 1965, **16**, 351–360.
- 20 G. Round and V. K. Garg, 1986.
- 21 M. Spiga and G. Morino, *International communications in heat and mass transfer*, 1994, **21**, 469–475.
- 22 S. Das, A. Garg, A. I. Campbell, J. Howse, A. Sen, D. Velegol, R. Golestanian and S. J. Ebbens, *Nature communications*, 2015, **6**, 8999.
- 23 J. Simmchen, J. Katuri, W. E. Uspal, M. N. Popescu, M. Tasinkevych and S. Sánchez, *Nature Communications*, 2016, **7**, 1–9.
- 24 D. Giacché, T. Ishikawa and T. Yamaguchi, *Physical Review E*, 2010, **82**, 056309.
- 25 B. Sabass and U. Seifert, *The Journal of chemical physics*, 2012, **136**, 214507.
- 26 S. B. Hall, E. A. Khudaish and A. L. Hart, *Electrochimica Acta*, 1998, **43**, 579–588.
- 27 J. R. Howse, R. A. Jones, A. J. Ryan, T. Gough, R. Vafabakhsh and R. Golestanian, *Physical review letters*, 2007, **99**, 048102.
- 28 W. Wang, T. Y. Chiang, D. Velegol and T. E. Mallouk, *Journal of the American Chemical Society*, 2013, **135**, 10557–10565.
- 29 A. Zöttl and H. Stark, *Physical review letters*, 2012, **108**, 218104.
- 30 J. Katuri, W. E. Uspal, J. Simmchen, A. Miguel-López and S. Sánchez, *Science advances*, 2018, **4**, eaao1755.
- 31 A. Sokolov and I. S. Aranson, *Nature communications*, 2016, **7**, 11114.
- 32 S. J. Ebbens and J. R. Howse, *Soft Matter*, 2010, **6**, 726–738.
- 33 G. M. Whitesides and B. Grzybowski, *Science*, 2002, **295**, 2418–2421.
- 34 I. S. Aranson, *Physics-Uspekhi*, 2013, **56**, 79.